Astroparticle Physics 31 (2009) 24–36

Contents lists available at ScienceDirect

Astroparticle Physics

journal homepage: www.elsevier.com/locate/astropart

Measurement of some EAS properties using new scintillator detectors developed for the GRAPES-3 experiment

The GRAPES-3 Collaboration: P.K. Mohanty [a], S.R. Dugad [a], U.D. Goswami [a], S.K. Gupta [a,*], Y. Hayashi [b], A. Iyer [a], N. Ito [b], P. Jagadeesan [a], A. Jain [a], S. Karthikeyan [a], S. Kawakami [b], M. Minamino [b], S.D. Morris [a], P.K. Nayak [a], T. Nonaka [b], A. Oshima [b], B.S. Rao [a], K.C. Ravindran [a], H. Tanaka [a], S.C. Tonwar [a]

[a] Tata Institute of Fundamental Research, Mumbai 400005, India
[b] Graduate School of Science, Osaka City University, Osaka 558-8585, Japan

ARTICLE INFO

Article history:
Received 10 September 2008
Received in revised form 29 October 2008
Accepted 9 November 2008
Available online 27 November 2008

PACS:
96.50.S–
96.60.sd
95.55.Vj
29.40.Gx

Keywords:
Cosmic rays
Extensive air shower
Particle detector
Scintillation detector

ABSTRACT

The GRAPES-3 extensive air shower (EAS) array started operation with 256 scintillator detectors at Ooty in India. Each detector is viewed by a fast photomultiplier tube (PMT) mounted at a height of 60 cm above the scintillator. However, for further expansion of the array, an alternative readout of the scintillator using wave-length shifting (WLS) fibers is employed. This resulted in improved performance with a larger photon signal and a more uniform response. With the inclusion of a second PMT, the dynamic range for particle detection has been increased to $\sim 5 \times 10^3$ particles m^{-2}. We now use plastic scintillators, developed in-house to cut costs. The measurement of the density spectrum, shows a power law dependence with an index $\gamma = 1.57 \pm 0.04$. Using the zenith angle dependence of the density spectrum, an attenuation length $\Lambda_a = 98$–106 g cm^{-2} for the EAS is obtained. These measurements are found to be consistent with the results reported earlier by other groups.

1. Introduction

The GRAPES-3 (**G**amma **R**ay **A**stronomy at **P**eV **E**nergie**S** – phase **3**) is a high density extensive air shower (EAS) array designed for precision study of the cosmic ray energy spectrum and its nuclear composition using the muon multiplicity distribution [1] in the energy range from 3×10^{13} eV to 3×10^{16} eV. The experiment was started with 256 plastic scintillator detectors (each 1 m^2 in area) deployed on a hexagonal pattern, at Ooty (2200 m altitude, 11.4°N, 76.7°E) in southern India in 2001. The scintillator detector is viewed by a fast photomultiplier tube (PMT) in a conventional configuration; wherein the PMT is mounted with its photo-cathode face at a height of 60 cm, above the scintillator. The entire assembly of scintillator and PMT is housed inside a highly reflecting trapezoidal shaped light-tight aluminum container [2]. The GRAPES-3 array also contains a large area (560 m^2) tracking muon telescope [3] to detect and measure the muon component in the EAS. The muon telescope is an effective tool, in the study of the nuclear composition of primary cosmic rays. The tracking muon telescope has also proved to be an invaluable tool in the studies of the solar flares, coronal mass ejections and the subsequent Forbush decrease events observed at the Earth [4,5].

The occurrence of the '*knee*' in the cosmic ray energy spectrum around 3×10^{15} eV is believed to be intimately related to the issue of cosmic ray origin. But even after several decades of study, a clear understanding of the origin of the '*knee*' is yet to emerge. Clearly the data obtained with higher sensitivity and lesser uncertainty in the estimation of the primary energy and the composition are expected to provide a better understanding of this important feature of the high energy astrophysics.

An efficient detector system should provide a large separation between the PMT noise and the signal due to the charged particles in the EAS, and should also have a uniform spatial response over the entire area of the scintillator. In the original GRAPES-3 trapezoidal shaped detectors, the scintillation photons collected at the PMT are, primarily due to diffuse reflection from the inner walls of the container [2]. This is not an efficient process, and results in a sizable loss of the signal. Most of the scintillator detectors had a photon output $\lesssim 10$ photo-electrons, even for the 5 cm thick

* Corresponding author. Tel.: +91 9869439435; fax: +91 2222804610.
E-mail address: gupta@grapes.tifr.res.in (S.K. Gupta).

0927-6505/$ - see front matter © 2008 Elsevier B.V. All rights reserved.
doi:10.1016/j.astropartphys.2008.11.004

scintillators used. The geometry of the detector also resulted in a large spatial non-uniformity in the signal across the detector and a variation ~30% is observed in photon output from the center to the edge of the detector. In view of these limitations, we have investigated the use of wave-length shifting (WLS) fibers [6,7] for an efficient collection of photons.

Observation of the photon pulses with a decay time of a few nanoseconds in plastic fibers were reported in 1981 [8] and subsequently, extensive development of the plastic fibers occurred. Use of WLS fibers, where wave-length shifting cores ranging from several hundred microns to a few mm diameter, surrounded by single or multiple layers of cladding of progressively lower refractive indices were developed. The double clad WLS fibers provide readout of the blue photon emitting scintillators in a detector, with the subsequent re-emission of the photons in the green wave-length using a 3-hydroxyflavone (3HF) type wave-length shifter present in the core material [9]. A fraction of the re-emitted photons are transported to the end of the fiber through total internal reflections. It is known that the double clad fibers provide an improved photon yield of up to 70% higher than the single clad ones, by increasing the fraction of light trapped through total internal reflections [10].

We have developed a new scintillator detector with significantly improved performance, by a suitable placement of the WLS fibers in machined grooves on the scintillator surface. Since, the spatial uniformity and the response time of the scintillator critically depends on the layout of the fibers, the performance of the detector has also been simulated using a Monte Carlo simulation code 'G3ScSIM' developed by us. A direct comparison of the results from the simulations and the actual measurements has allowed, a better understanding of the performance of the detector to emerge. Three different layouts of WLS fibers were evaluated using Monte Carlo code, G3ScSIM. However, the final configuration has been adopted on the basis of cost effective fabrication with excellent uniformity and high photon output. The saturation of the PMTs encountered at very high particle densities in the earlier GRAPES-3 detectors, limited their use over a wider range of primary cosmic ray energies. To overcome this limitation, the WLS fiber detectors have been designed with two PMTs. The results of the tests and the performance of the new detectors is summarized here.

The density distribution of the particles observed in an EAS detector station provides a useful and simple method of probing the energy spectrum of the primary cosmic rays. The integral density spectrum is defined as the frequency $N(\rho)$ with which the particle density exceeds a value ρ at a given location. To a first approximation the density spectrum $N(\rho)$ is given by,

$$N(\rho) = K \times \rho^{-\gamma} \quad (1)$$

However, the actual measurements have shown that γ is only approximately constant and it shows a very weak dependence on the detected particle density. Nevertheless, for most purposes a constant value of γ provides an adequate description of the data. If all EAS have an identical lateral distribution, the density spectrum represented by Eq. (1) implies a similar size spectrum of EAS [11]. The measurements of the density spectrum have shown a clear power law dependence as outlined above. The density spectrum obtained from a plastic scintillator detector at an altitude of 2770 m at Mt. Norikura showed a dependence of $N(\rho) = K \times \rho^{-\gamma}$; where $\gamma = 1.55 \pm 0.05$ was obtained in the density range 50–10^4 particles m^{-2}, which progressively increased to 2.0 at the densities beyond 2×10^4 particles m^{-2} [12].

The zenith angle distribution of the EAS has been studied for a long time to measure the attenuation of the EAS in the atmosphere [13,14]. The zenith angle distribution of the EAS for different particle densities has been used to estimate the attenuation length of the EAS by the ARGO–YBJ collaboration. They have reported an attenuation length of (124 ± 11) g cm^{-2} in Tibet, at an atmospheric depth of 606 g cm^{-2} [15]. The KASCADE collaboration has studied the attenuation of the EAS in great detail at the sea level, and have obtained a value of (100–120) g cm^{-2} for this parameter [16]. Although, a direct comparison of the above two experimental results is rather difficult, owing to the different altitudes of observation and radically different methods of data analysis employed. However, the fact that the magnitude of the attenuation length are same within stated errors, indicates that it is very useful parameter to describe the attenuation of EAS in the atmosphere.

2. The experimental setup

A special experimental setup has been erected, for studying the performance of the scintillator detectors being developed. A sketch of the arrangement used in this setup, consisting of three sets of trigger scintillators is shown in Fig. 1. The two scintillator hodoscopes are placed, directly above and below the scintillator detector under development. Each hodoscope consists of a total of 10 strips of plastic scintillators, each strip is 50 cm long with a cross-sectional area of 10 cm × 2 cm. The 10 strips are divided into two groups of 5 strips each. The first group of 5 strips labeled U1 through U5, are placed adjacent to each other to form a layer, covering an area of 50 cm × 50 cm, seen as the top layer in Fig. 1. The second group of 5 strips labeled L1 through L5, are also similarly deployed, but along a direction orthogonal to the first group. Each strip is viewed by an individual 5 cm diameter, fast PMT (model ETL-9807B) coupled directly to the strip. To avoid the cross-talk, each strip is wrapped in aluminum foil and then inside a layer of black plastic sheet. The high voltage applied to each PMT is adjusted, to make it fully sensitive to single muons. Thus, each hodoscope records the passage of a through going muon by the two groups of scintillator strips along two orthogonal, namely *X*- and *Y*-directions to a precision of 10 cm × 10 cm. A total of 25 localized cells, of constant cross sectional area (10 cm × 10 cm) are obtained from each hodoscope as is shown in Fig. 1. A vertical separation of 50 cm between the two hodoscopes allows the direction and the location of each muon to be determined.

In addition, another plastic scintillator (50 cm × 50 cm × 5 cm in size) is placed below the lower hodoscope, inside an inverted, trapezoidal shaped cone, with inner surfaces painted black. The PMT viewing this scintillator is placed at the bottom of the cone, which detects only direct photons, thus providing significantly better timing.

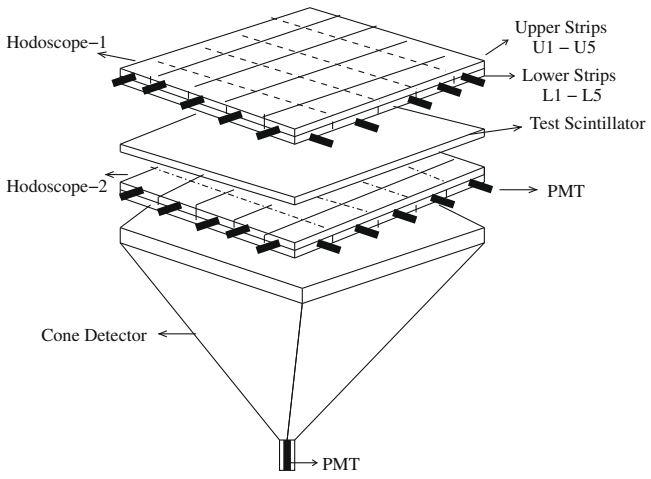

Fig. 1. A sketch of the experimental setup with two identical hodoscopes placed, above and below the test scintillator along with the trapezoidal shaped detector.

The muon trigger is generated as described below. As shown in Fig. 2, the output pulses from each of the PMTs coupled to the 10 strips from the 2 layers of a hodoscope, are discriminated to produce logical output pulses. Next, a logical OR of the discriminator outputs, from the 5 strips in a layer called OR1 is generated which indicates the passage of a muon through layer 1 in hodoscope 1. Thus the 4 layers of the scintillator strips from the two hodoscopes provide 4 independent signals OR1, OR2, OR3, OR4 during the passage of a muon. Finally, a 4-fold coincidence of OR1, OR2, OR3, OR4 is taken to generate the initial muon trigger μ_0. The output of the PMT from the trapezoidal shaped detector is also discriminated and its coincidence is taken with μ_0 after a small delay, to generate trigger μ_1. Signal μ_1 provides faster timing, because the trapezoidal shaped detector triggers only on direct photons which have significantly smaller time spread. Signal μ_1 is subsequently also used as the GATE for the charge integrating analog to digital converters (ADCs) and as the START for the time to digital converters (TDCs). Since μ_1 is generated by a 5-fold coincidence, it provides a relatively clean muon trigger, free from the noise in the PMTs.

The passage of the muons through the specific scintillator strips in the two hodoscopes is obtained, by latching the discriminator output pulses from all 20 strips as a flag by the use of a 20-bit flag latch module, where the corresponding bit for the strip is set to the logical state '1' if that strip is hit, otherwise it is set to the state '0'. Normally a muon would results in at least 4 strips being hit from the 4 layers of scintillators in the two hodoscopes. A small fraction of the total events record hits in more than one strip in a single layer, which might be due to the passage of an inclined muon, through two adjacent strips or due to the production of a knock-on electron by the parent muon. Events with such multiple hits are rejected during the subsequent data analysis.

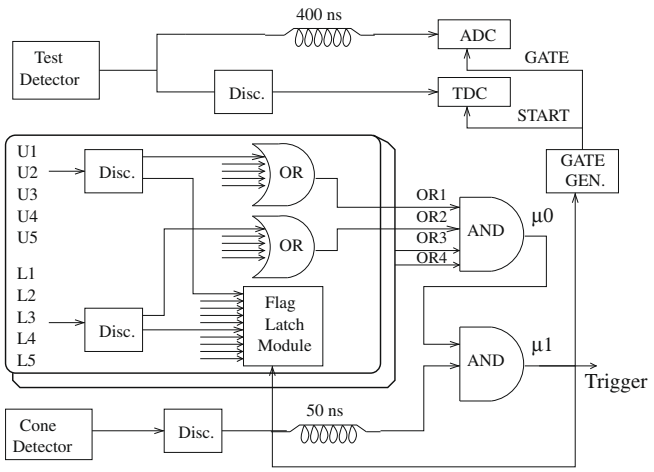

Fig. 2. A schematic diagram of the trigger and signal processing setup used in the measurements.

The information on the scintillator strip hits are used to localize the muons to within cells of 10 cm × 10 cm in size, as shown in Fig. 1. However, only near vertical muons are selected for further analysis. To obtain a reasonably good statistics, the data are accumulated over a period of 7 days. The ADC and the TDC distributions are obtained for each of the 25 position cells (10 cm × 10 cm in size). These ADC and TDC distributions are then compared with the results of the Monte Carlo simulations. The PMT viewing the test detector has been calibrated by measuring its response to single photons, which is shown in Fig. 3. The observed first photo-electron peak has been fitted to a Gaussian function. The width of this fit is used in the subsequent Monte Carlo simulations to generate the PMT response.

In the present study, Kuraray double clad WLS fibers of type Y11 (200) [17] have been used. These 1 mm diameter fibers consist of a central polystyrene core (refractive index $\eta = 1.59$) with two outer claddings of progressively lower refractive indices. The inner cladding is polymethyl-methacrylate (PMMA) with $\eta = 1.49$ and the outer cladding is fluorinated polymer (FP) having $\eta = 1.42$. All fibers are cut to a length of 1.3 m. To place the WLS fibers inside the scintillator, 1.5 mm wide and 2 mm deep grooves have been machined on the surface of the scintillator (50 cm × 50 cm × 2 cm). Three different groove designs named, '*parallel*', '*matrix*' and 'σ' have been investigated. The layout of these 3 designs are schematically shown in Fig. 4. Since the *parallel* and *matrix* grooves are straight, they are machined using an ordinary milling machine. However, the σ grooves require the use of a CNC milling machine.

For the *parallel* and the *matrix* configurations, a total of 12 grooves with equal inter-groove separation are machined. An inter-groove separation of 4.0 cm is used for the *parallel* grooves (50 cm long) as shown in Fig. 4a. For the *matrix* grooves the separation is 9.6 cm, for the two mutually orthogonal sets of 6 grooves (50 cm long), as shown in Fig. 4b. A total of 16 σ grooves are machined, each 41 cm long as seen in Fig. 4c. The total length of the WLS fibers embedded in the scintillator is 900 cm in the cases of the *parallel* and the *matrix* groove configurations. The WLS fiber

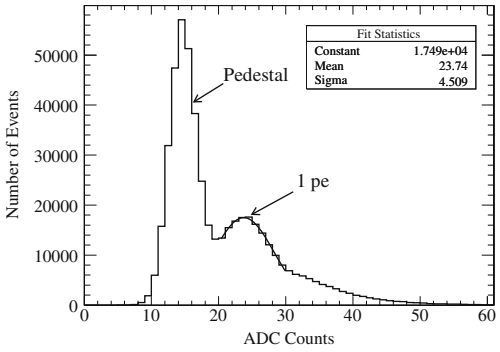

Fig. 3. Single photo-electron response of the PMT used in the test scintillator. A Gaussian function is fitted to the first photo-electron peak.

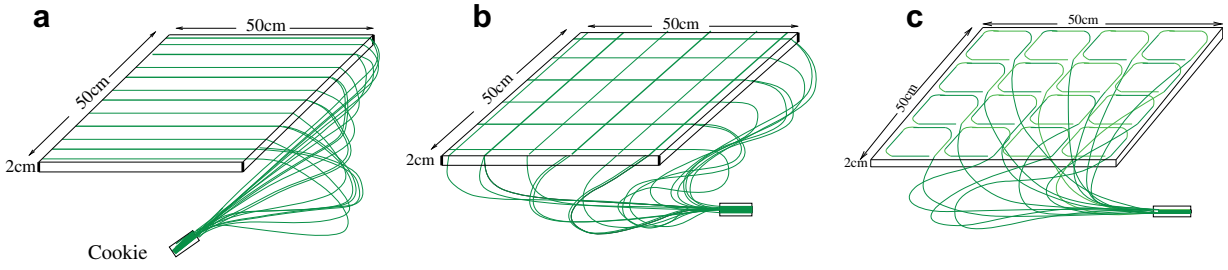

Fig. 4. The three groove layouts on the scintillator surface with embedded WLS fibers (a) *parallel*, (b) *matrix*, and (c) σ.

are restrained from any movement by applying tiny strips of adhesive aluminum tape just above the groove. A total of 18 fibers have been used and placed in alternative grooves as single and two fibers, respectively. The total length of WLS fibers is 656 cm for the σ configuration with only one fiber in each groove as shown in Fig. 4.

The entire scintillator and WLS fiber assembly is wrapped inside two layers of Tyvek paper [18], which acts as an efficient but diffuse reflector, resulting in a substantial enhancement in the number of the photons collected. Tyvek has been chosen for its high reflectivity, chemically inert nature and excellent mechanical strength. Since only a small fraction of the total length (41 or 50 cm) of WLS fiber is embedded inside the groove, the remainder is used for its smooth and safe bending, en-route to the PMT. The free ends of the WLS fibers are bunched together and glued into an acrylic disk called a 'cookie' which is finally coupled to the PMT using an optical glue. The entire assembly is placed inside a light-tight aluminum tank. The experimental conditions are kept unchanged during the tests with different groove designs.

3. Monte Carlo simulations (G3ScSIM Code)

Prior to the actual experimental measurements, a Monte Carlo simulation code 'G3ScSIM' [19] has been developed to get an understanding of the response of the scintillator for different fiber configurations. The G3ScSIM is basically a photon tracking code, for a plastic scintillator of rectangular geometry, with embedded WLS fibers of cylindrical geometry. In this code, the trigger conditions are kept identical to those in the experiment with cosmic ray muons, as shown in the Fig. 1. The important input parameters used in G3ScSIM are listed in Table 1. Some of the simplified assumptions made in G3ScSIM are: (i) the scintillator response is homogeneous, (ii) the scintillator photons are monochromatic, and (iii) the WLS fibers are in optical contact with the scintillator surface, over an area projected by it. A brief description of some of the relevant features of G3ScSIM code are summarized below and described in greater detail elsewhere [19].

3.1. Basic G3ScSIM code

The detector setup modeled in G3ScSIM code, is identical to that in Fig. 1. The origin of the coordinate system is selected at the corner of the test detector and the geometry is defined through its extreme coordinates (X_{min},Y_{min}) to (X_{max},Y_{max}). The cosmic ray muons are generated over the surface of the top hodoscope (Fig. 1) with random coordinates x, y and arrival direction; zenith angle θ ($0 \leqslant \theta \leqslant 60\,^\circ$), azimuth angle ϕ ($0 \leqslant \phi \leqslant 360\,^\circ$). By projecting the trajectory of the muon, its location on the test detector, and on the other triggering detectors is calculated. A trigger is generated, only if a muon passes through all the five triggering detectors.

The energy loss $-dE/dx$ of the muon, in the test scintillator is calculated using the Landau distribution [20,21] based on an algorithm from the CERN library [22]. The computed energy loss distribution of vertical muons in a 1 cm thick scintillator is shown in Fig. 5, assuming a mean energy loss of 1.89 MeV/g cm^{-2}, for relativistic muons [23]. A production rate of one short wave-length (blue) photon per 100 eV energy loss is assumed. The blue photons are generated along the track of the muon, every 0.1 mm, with the emission angles θ and ϕ, selected randomly from an isotropic angular distribution. The emission time of each photon is calculated from an exponential distribution with a decay time of 1.7 ns for the scintillator, as measured by us earlier.

The propagation of the blue photons in the scintillator is tracked, by a ray tracing method, governed by the laws of geometrical optics [24]. The incidence of a photon on the scintillator surface is determined, from among the six surfaces of the scintillator. At every reflection from the scintillator surface, three possibilities exist, namely; (i) the absorption of the photon in the scintillator, (ii) the interception by a WLS fiber, and (iii) the reflection from the scintillator surface. To determine absorption of a photon in the scintillator, the total path-length traversed is compared with the survival path-length for that photon, using the Monte Carlo technique.

Normally a photon incident on the scintillator surface at an angle greater than the critical angle, would undergo total internal reflection from a flat surface. However, the scintillator surface is not perfectly flat and any departure from the flatness would result in the escape of the photon. This effect is taken into account by assuming an effective total internal reflectivity (ETIR) <100%. The exact value of ETIR is determined empirically as described below. The Tyvek wrapping of the scintillator provides an efficient and diffuse reflecting surface of known reflectivity, for the photons escaping from the scintillator back into the scintillator. The photon reflection probability from the diffuse reflector is calculated using the Lambert's cosine law [25], where the angle of reflection is independent of the incident angle. However, when the scintillator is wrapped inside a black plastic sheet, the reflectivity from its surface of escaped photons is assumed to be zero.

To determine the incidence of a photon on the WLS fiber, we assume the area projected by the fiber on the scintillator surface as the overlap area. If a photon is incident on the overlap area, it is deemed to be absorbed by the fiber. Subsequently, a new longer wave-length (green) photon is generated with a wave-length distribution derived from the emission spectrum of WLS fiber, and tracked in case of trapping in the fiber, using critical angle condition. At this point, a new start time is generated from the measured decay time (6.1 ns) of the WLS fiber. This in turn is added to the

Table 1
Monte Carlo simulation parameters.

Scint. Refractive index (η_{sc})	1.59
WLS (η_{wls}) Fx core 1.59	
In. clad	1.49
Out. clad	1.42
Scint. decay time	1.7 ns
WLS fiber decay time	6.1 ns
Scint. attenuation length	100 cm
WLS attenuation length	350 cm
Tyvek reflectivity	90%
ETIR	93%
PMT time jitter (FWHM)	2.2 ns
Mean energy loss/photon	100 eV

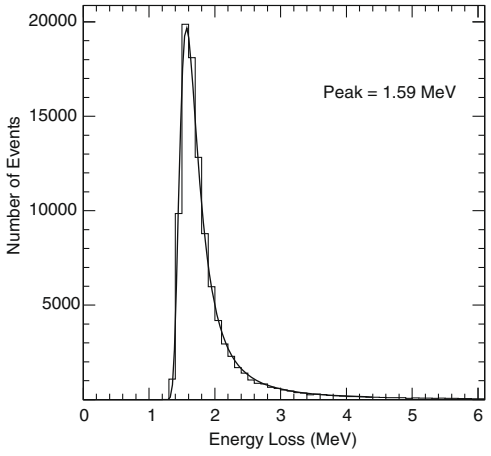

Fig. 5. Energy loss distribution of vertical muons in a 1 cm thick scintillator. Mean energy loss = 1.89 MeV. A Landau distribution fit gives a peak at 1.59 MeV.

earlier transit time of the blue photon, from the time it was generated in the scintillator to the time of its absorption in the fiber. A trapped green photon is propagated, until it is absorbed in the fiber due to attenuation or if it reaches the collection end of the fiber. The green photons propagating in the direction opposite to that of the PMT are assumed to be lost. The green photons reaching the PMT are converted into photo-electrons at the photo-cathode using the wave-length dependent quantum efficiency of the PMT. The amplitude and the response time of the PMT are convoluted to generate the PMT pulse. For each muon, the recorded information includes the *X*, Y coordinates on the triggering and test scintillators, also the photon statistics such as the number of photons (i) produced in the scintillator, (ii) escaped from the scintillator, (iii) lost due to the attenuation, (iv) absorbed in the WLS fiber, (v) escaped from the fiber, and finally the number of the photo-electrons and their arrival times at the PMT.

3.2. Effective total internal reflectivity (ETIR)

A Monte Carlo simulation can reproduce the experimental data only if the detector parameters describing its performance are sufficiently close to their true values. These parameters include the scintillation efficiency, the surface reflectivity, the attenuation length, and the decay times etc. Many of these parameters have been directly measured by us or are available from the literature. The remaining parameters have to be obtained by assuming some initial values and then fine tuning those values by matching the simulation results with the experimental data for a particular configuration of the test detector. The results can then be cross checked by carrying out another set of measurements with a different configuration of the test detector.

To fix the free parameters in the simulations, the *parallel* groove design, with and without the Tyvek wrapping was modeled. The only free parameter used in these simulations is the ETIR. The initial value of the ETIR is taken to be 100%, implying that the scintillator surfaces to be perfectly flat. The resultant photon distribution from the simulations disagreed with the experimental data. It is observed that the simulated ratio of the mean number of photons with and without the Tyvek wrapping is 2.2, while the experimental value is 3.3. It is observed that this ratio increases with decreasing value of ETIR. A value of ETIR = 93%, gives a nearly perfect agreement with the experimental data. This value of the ETIR has been used for all subsequent simulations.

3.3. Photon statistics

The muons suffer a mean energy loss of 1.89 MeV/cm in a scintillator. However, when due account is taken of the muons arriving from different directions that trigger the setup, the mean energy loss becomes 4.6 MeV in the 2 cm thick scintillator used. This results in production of a large number of photons (~46,000), but only a small fraction is eventually received by the PMT. The simulations show that ~86% of the produced (blue) photons are either absorbed or escape from the scintillator. The mean path-length traversed by the blue photons is ~51 cm and the mean number of reflections is ~14 inside the scintillator. Therefore, ~14% of blue photons manage to enter the WLS fiber, which after initial absorption are re-emitted as green photons. Furthermore, because of the large value of the critical angle, most of the green photons escape from the WLS fibers, and only ~14% of the photons are trapped. These photons travel along both directions in the fiber. The mean path-length traversed by green photons is ~112 cm and the mean number of reflections is ~430 prior to reaching the PMT. Finally, only ~0.45% of the total photons produced in the scintillator, namely ~208 photons arrive at the PMT.

4. The detector design

The main design goal for the new detector is to efficiently record shower particles over a large dynamic range (1–10,000 particles), to cover a wide range in the energy spectrum of the primary cosmic rays from $\sim 10^{13}$, where the particle density at the core is rather small; to $\sim 10^{17}$ eV where densities may reach several thousand particles m^{-2}. Efficient detection of a single or a few particles is ensured by designing a detector with high photon yield and good spatial uniformity. The high photon yield also implies that the PMT may be operated at a relatively lower voltage, thereby reducing the noise and increasing its life. The PMTs are typically operated at a gain of $(3–5) \times 10^6$, which is within the recommended region specified by the manufacturer. However, at high particle densities, the anode current become very large and the PMT response become non-linear. For the ETL-9807B PMT used here, the response becomes non-linear at a peak anode current of 50–150 mA. This translates into the onset of the non-linearity at $\gtrsim 50$ particles and of saturation at ~100–200 particles. This introduces error in the estimation of the various shower parameters. Although, one can use the signal from an earlier stage of the dynode chain to avoid saturation, we prefer to employ a second PMT to enhance the dynamic range of our detectors.

As described below, through a study of the; (i) photon output, (ii) uniformity and (iii) the time response for different groove designs, we find that the simple and inexpensive *parallel* groove configuration meets our design goals. Using 4 scintillator tiles, a 1 m^2 detector has been fabricated. The side-view of a complete dual-PMT WLS fiber detector is shown in Fig. 6. The single-PMT fiber detector is identical to a dual-PMT detector, except that it is operated with only one high-gain PMT. The photons from each 50 cm × 50 cm scintillator tile are collected by 18 fibers for the high-gain PMT, whereas only 6 fibers are used for the low-gain PMT. The groups of 18 and 6 fibers for the high- and low-gain PMTs are placed inside 12 grooves, as has been described in the Section 2. Two groups of fibers from the 4 scintillators are coupled to two

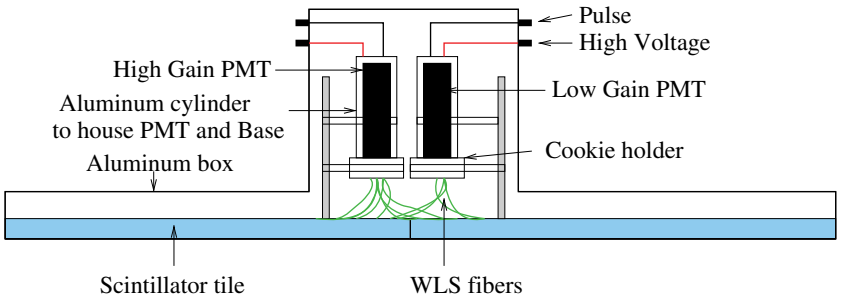

Fig. 6. Side-view of dual-PMT fiber detector. Total number of fibers from the scintillator to high-gain PMT is 72 and to low-gain PMT is 24.

PMTs, through two separate cookies; the first containing $18 \times 4 = 72$ fibers to the high-gain PMT, and the second $6 \times 4 = 24$ fibers to the low-gain PMT.

The PMT is placed inside an aluminum cylinder to shield it from external electrical noise. The two PMTs are vertically mounted at the center of an aluminum tank of dimension 112 cm × 103 cm × 5 cm as shown in Fig. 6. This detector is more compact, lighter, and easier to maintain, as compared to the old trapezoidal design. The fabrication of the dual-PMT fiber detectors started in 2004, and about 100 such detectors have been fabricated and successfully deployed in the array. These detectors are placed every 16 m, starting from the center of the array, by replacing the corresponding old trapezoidal shaped detectors.

5. Discussion

5.1. Photon yield

The reflecting surfaces play a key role in obtaining a higher photon yield and a better uniformity. Thus a quantitative comparison has been done both, without and with a reflecting Tyvek wrapping, using a scintillator with *parallel* grooves. The measured photo-electron distributions are shown in Fig. 7: (a) with a black plastic wrapping to prevent any reflection of the photons escaping from the scintillator back into it and, (b) with two layers of Tyvek wrapping to ensure efficient reflection of the escaped photons back into the scintillator.

Both distributions are asymmetric and display the characteristic Landau tail. Therefore a convoluted Landau with a Gaussian fit (http://root.cern.ch/root/html/examples/langaus.C.html) has been used, to estimate the peak values. The peak values provide a measure of the scintillator photon output. The peak is at 6.4 photo-electrons with the black plastic sheet wrapping and 20.5 photo-electrons with Tyvek wrapping. Thus the ratio of the photon output with the Tyvek and the black plastic wrapping is 3.2 for the scintillator with *parallel* grooves.

A comparison of the photo-electron distributions for the *parallel*, the *matrix*, and the σ groove designs for the experimental data and the Monte Carlo simulations are presented in Fig. 8, and the results are also summarized in Table 2. Here it needs to be emphasized that the simulation parameter 'ETIR' has been extracted, using only the *parallel* groove data and then subsequently used for the *matrix* and the σ grooves. An excellent agreement between the photo-electron distributions from the data with the Monte Carlo simulations for the remaining two designs namely the *matrix* and the σ is seen in Fig. 8. Further, it can be seen from the Table 2 that the photo-electron yield in the case of the *parallel* groove is comparable to that of the *matrix* groove, whereas it is significantly lower in the case of the σ groove. The embedded length of the fibers in the σ groove is 27% less, as compared to the other two groove designs, however, the photo-electron yield in the σ groove is 13% less as compared to the *parallel* groove and 18% less compared to the *matrix* groove. Thus the photo-electron yields per unit length of the embedded fiber, for the three groove designs are comparable to within ~10%, irrespective of the shape and the layout of the grooves. Based on these results, it has been decided to

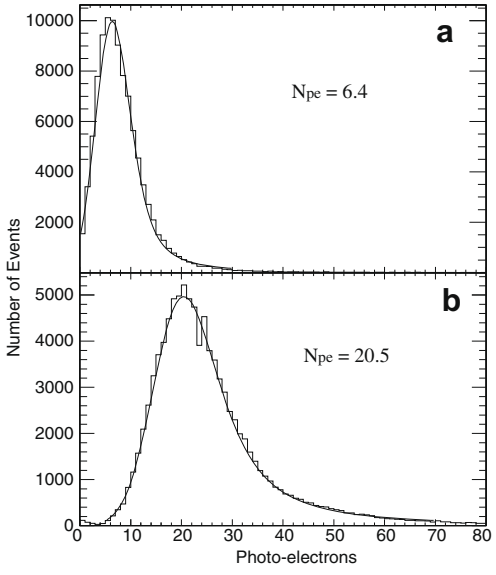

Fig. 7. Photo-electron distribution from muons in *parallel* grooved detector wrapped in (a) black plastic, (b) two layers of Tyvek. Fits to a convoluted Landau with Gaussian yields, peak at (a) 6.4 and (b) 20.5 photo-electrons.

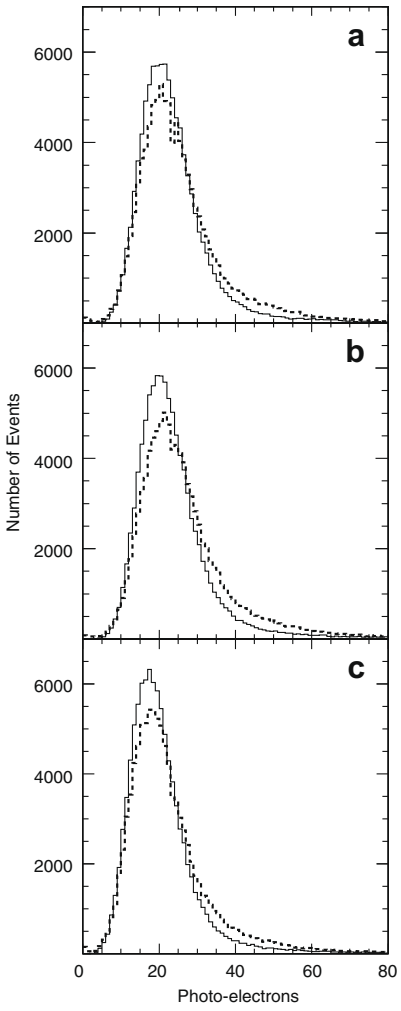

Fig. 8. Photo-electron distributions: (a) *parallel* groove, (b) *matrix* groove, and (c) σ groove. Experimental data shown by dashed line and Monte Carlo results by continuous line.

Table 2
Photo-electron yield of scintillator for different WLS fiber configurations.

Groove	Fiber-length (cm)	Photo-electrons
Parallel	900	20.5
Matrix	900	21.7
σ	656	17.9

employ the *parallel* groove configuration, since it is economical to implement and the assembly of the detector is also relatively simpler.

To measure the photo-electron yield as a function of the number of the WLS fibers, we used a scintillator with *parallel* grooves with 3, 6, 9, 12 and 18 fibers. Different number of fibers were accommodated in the 12 grooves on the scintillator surface, by distributing them in a uniform manner. The photo-electron yield for each of these five configurations is also simulated. The experimental data and the simulation results are shown in Fig. 9. It is seen that the photo-electron yield increases linearly with the number of fibers and there is good agreement between the data and the simulations. For the ease of estimating the number of detected photo-electrons, a linear relation is fitted to the experimental data by

$$N_{pe} = a + bN_F, \tag{2}$$

where N_{pe} is detected number of photo-electrons, N_F the number of WLS fibers. The linear fit to the experimental data yields the values of the; intercept $a = (-0.1 \pm 1.0)$ and the slope $b = (1.12 \pm 0.09)$. As seen from Fig. 9 this fit also provides an adequate description of the simulation results.

5.2. Detector uniformity

The photon output across the scintillator surface for the *parallel* grooves is shown in Fig. 10 as Lego plots, for the two cases of scintillator wrapped inside; (a) black plastic sheet, and (b) Tyvek paper respectively. In these plots, the vertical axis represents the relative photon yield in one of the 25 positions, and the highest value is normalized to 100. The *Y*-axis represents the longitudinal direction of the fibers in the scintillator, whereas the *X*-axis represents the transverse direction. In the case of the black plastic wrapping (Fig. 10a) two clear trends are observed namely a decrease in the photon output; (i) along the fiber, away from the PMT and (ii) from the central area towards the edge, along the transverse direction is seen. The first trend is due to the attenuation of the photons in the WLS fibers. This is because farther is the location of a muon from the PMT, longer is the length of the fiber that a photon has to travel prior to its detection, resulting in enhanced attenuation. The second effect may be due to the fact that, as the muon passes closer to the edge, the escape probability of the produced photons increases. With the Tyvek wrapping, the response is far more uniform as seen in Fig. 10b. Only a very small decrease is seen along the longitudinal direction of the fibers. The response near the edge is also higher than in the central area. This behavior is opposite of the case with the black plastic wrapping. This may be due to the reentry of the escaped photons at the edges, due to the reflections from the Tyvek surface, back into the scintillator. The Tyvek wrapping also increases the photon yield by a sizable factor (3.2) besides improving the uniformity of the detector response.

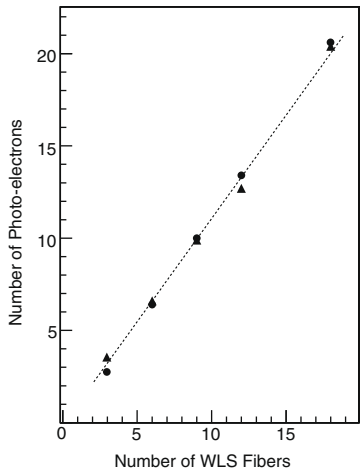

Fig. 9. Variation in detected photo-electrons as a function of number of WLS fibers: (a) ▲ experimental data, (b) • Monte Carlo results. Dashed line is linear fit to experimental data.

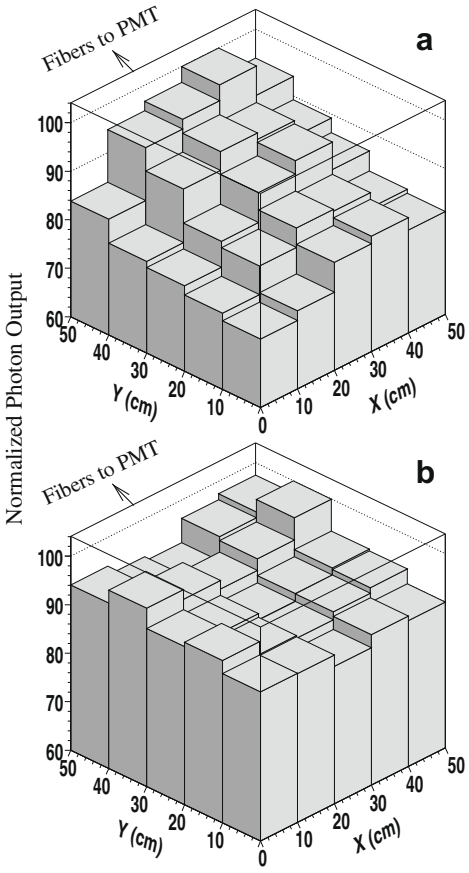

Fig. 10. Normalized photon output for *parallel* grooves: (a) with black plastic wrapping, (b) with two layers of Tyvek wrapping.

The variation in the response, across the scintillator surface for all the three groove designs with Tyvek wrapping, are shown in Fig. 11 as Lego plots. In the case of the *parallel* groove, a small decrease in the photon output is observed, from near the PMT end to the far end of the fiber. In the *matrix* groove, a similar trend with reduced magnitude is seen. However, in the case of the σ groove, no such variation is observed. Also no transverse variation in the photon output is observed for the *matrix* and σ grooves, whereas for the *parallel* groove the edge response is slightly higher than from the central area as stated above.

The photon output variation in the longitudinal direction of the fiber is calculated by averaging the data in the transverse direction and the results are presented in Fig. 12 for a comparison with the simulations. In Fig. 12a for the *parallel* grooves both simulation and data show a decrease ~5% in the photon output, over a distance of 50 cm, on the other hand, in the case of *matrix* grooves (Fig. 12b) there is a smaller drop (1–3)% in the central region as compared to the edge positions for both data and simulations. However, the situation is exactly reversed in the case of the σ grooves (Fig. 12c), where a small increase (1–3)% is seen.

The root mean square (rms) non-uniformity for the three groove designs is calculated separately, for both the data and the simulations and these are summarized in Table 3. The simulated

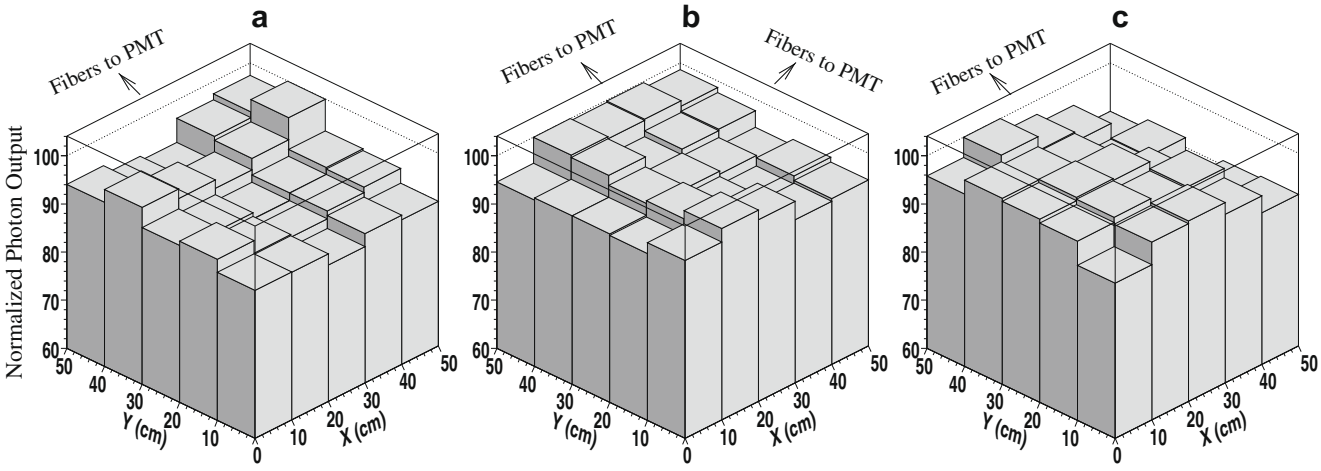

Fig. 11. Normalized photon output for (a) *parallel*, (b) *matrix*, and (c) σ grooves.

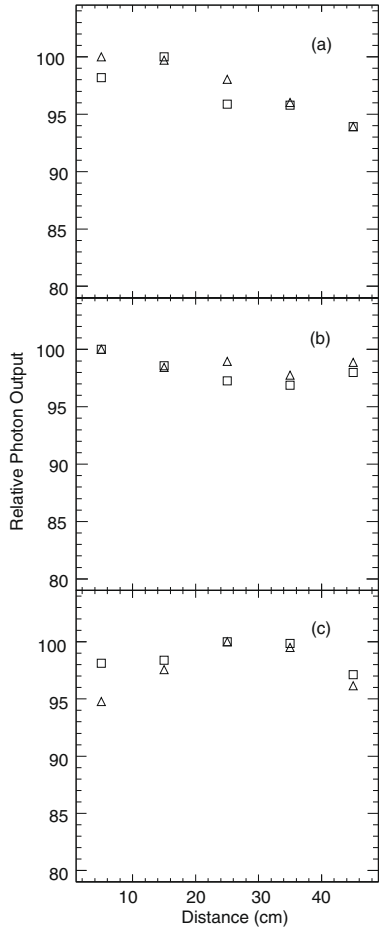

Fig. 12. Normalized photon output variation from near PMT to far end of the fiber for (a) *parallel*, (b) *matrix*, and (c) σ grooves. □ experimental data and △ Monte Carlo simulation.

values of rms non-uniformity is always slightly smaller (0.2–0.7)%, than the corresponding experimentally measured value for all the three designs. This is not surprising, in view of the fact that many of the assumptions in the simulations are only approximations to the real world. For example, any imperfections on the surface of the scintillator or any variations in its density, would result in enhanced rms non-uniformity in the experimental data. However,

Table 3
Uniformity in different groove patterns.

Groove type	RMS non-uniformity (%)	
	Experiment	Monte Carlo
Parallel	2.7	2.0
Matrix	2.1	1.6
σ	3.5	3.3

the rms non-uniformity is less than 4% for all three groove designs, well below our acceptable level of 5%.

5.3. Time response

The distribution of the time difference between the test scintillator and the trapezoidal shaped trigger detector is obtained from muons. It is measured using the setup shown in Fig. 1 and the trigger scheme shown in Fig. 2. The trapezoidal shaped detector at the bottom which has the fastest time response, provides the START and the test scintillator provides the STOP to the TDC. In the subsequent analysis the entire area (50 cm × 50 cm) of the detector is used, thereby incorporating the time differences, due to the propagation of the photons inside the scintillator as has been explained earlier in Section 2.

The measured time distributions for the three groove designs are shown in Fig. 13 by a dashed line and compared with the simulated distributions on the same plot which is shown by a continuous line. For this comparison the peak positions of the data and the simulated distribution were artificially aligned. This is acceptable because a fixed time offset has no physical significance. A reasonable agreement is observed between the widths of the time distributions for the data and the simulations. For the *parallel* grooves the full width at half maximum (FWHM) is 6.5 and 6.1 ns (Fig. 13a), for the *matrix* grooves the FWHM is 6.4 and 6.0 ns (Fig. 13b), and for the σ grooves the FWHM is 6.3 and 6.3 ns (Fig. 13c), for the experimental data and simulations, respectively. The values of the FWHM for the three groove designs agree to within ±0.2 ns. This shows that the time resolution is largely independent of the groove design.

The position dependence of the arrival time from the simulations indicates that the time difference between the far- and the near-end positions along the fiber is 1.7 ns in the case of *parallel* grooves and 1.0 ns for the *matrix* grooves. This may be understood as the transit time difference along the length of the fiber. The photons generated near the PMT will arrive earlier than those from the

far end, resulting in a finite transit time difference. However, for the case of the σ grooves, no variation in transit time is expected and none is observed.

A low photon detection threshold and a high photon yield are considered necessary for getting a good time resolution in a scintillator detector [26]. The effect of these two factors, on the time resolution has been quantitatively studied, through simulations. For this purpose the detector response, for the number of embedded fibers N_F = 6, 9, 12, 18 has been simulated. From these simulations we estimate the mean number of photo-electrons (N_{pe}) to be 6.4, 10.0, 13.4, and 20.6 for 6, 9, 12, and 18 embedded fibers respectively. The results of this study are shown in Fig. 14. The 4 plots in Fig. 14, clearly show that the time resolution improves with decreasing threshold. It is also clear that for a given threshold, increasing the number of fibers (N_F), results in a better time resolution. For smaller values of N_F, the time resolution changes linearly with the threshold, whereas the change is somewhat slower at higher values of N_F. For N_F = 6, the increase in the time resolution is 1.45 ns/N_{pe}, whereas it is only 0.13 ns/N_{pe} for N_F = 18. Thus the time resolution becomes less sensitive to the threshold for higher values of N_F. The time resolution can be improved either by increasing the photon output or reducing the threshold. However, the threshold level of the discriminator can not be arbitrarily reduced, due to the increased contribution to the count rate, from the PMT and other sources of noise.

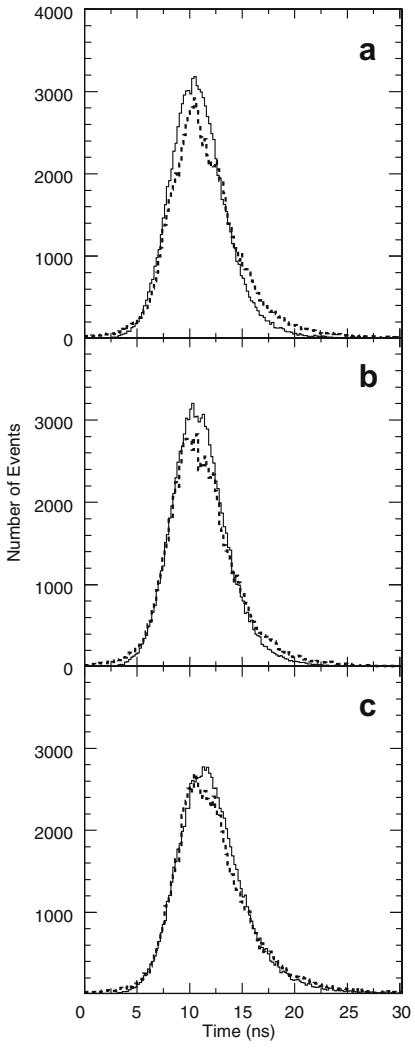

Fig. 13. Time response of the scintillator for (a) *parallel*, (b) *matrix*, and (c) σ groove. Experimental data is shown as dashed line and simulations by continuous line.

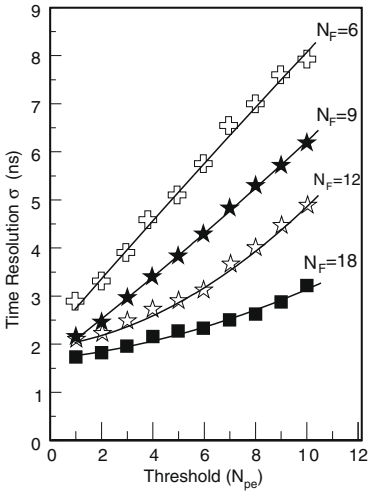

Fig. 14. Dependence of time resolution on photo-electron threshold as derived from simulations. Each plot is for a different number of embedded WLS fibers.

Encouraged by the good agreement in the time response observed between the data and the simulations, an effort has been made to understand the effects of various experimental factors influencing the time resolution, based on the simulations. The time resolution of the detector may be parametrized as follows:

$$\sigma_{total} = \sqrt{\sigma^2_{\tau_{sc}} + \sigma^2_{stat} + \sigma^2_{\tau_{WLS}} + \sigma^2_{PMT}} \quad (3)$$

where $\sigma_{\tau_{sc}}$ is the contribution to time resolution due to the decay time of the scintillator, σ_{stat} due to the statistical fluctuation in the number of detected photons, $\sigma_{\tau_{WLS}}$ is due to the decay time of WLS fiber, and σ_{PMT} is the contribution due to the transit time spread in the PMT. The Monte Carlo simulations have been performed for the *parallel* groove configuration with Tyvek wrapping. First, σ_{stat} is computed by setting all other decay times namely, τ_{sc}, τ_{WLS} and σ_{PMT} to zero in the simulations. The value of σ_{stat} is found to be 1.4 ns. Similarly $\sigma_{\tau_{sc}}$ is determined to be 1.0 ns and finally $\sigma_{\tau_{WLS}}$ is calculated to be 2.2 ns. These results imply that the largest contribution to the time resolution is due to the decay time of WLS fiber. This is not very surprising because the measured decay time of WLS fiber at 6.1 ns, as mentioned earlier, is the biggest contributor to the time resolution.

5.4. The detector performance

To compare the performance of the newly developed fiber detector with the old trapezoidal detector, about three months of the EAS data (1 March–29 May 2005) have been analyzed for both types of detectors. The PMTs used in the trapezoidal detectors are operated at a gain that is comparable to that of the high-gain PMT in the fiber detectors. During this period only 20, dual-PMT fiber detectors were operating and these were distributed starting from the center of the array, to right up to the 6th ring in the array. The GRAPES-3 air shower trigger system, the trigger criteria and the recording of the shower information have been described in detail elsewhere [2]. For the high-gain PMT in a dual-PMT fiber detector and the trapezoidal detector PMT, both the ADC and the TDC information is recorded, while for the low-gain PMT (dual-PMT detector), only the ADC data are recorded. The ADC data are converted into an equivalent number of minimum ionizing particles for each shower. Since the detector area is 1 m^2, the recorded number of particles in a detector represents the particle density in the detector.

The particle density in each detector is calculated by subtracting the concurrent pedestal value from the observed ADC count

and by dividing it with the single particle gain for that detector. The single particle calibration is performed periodically once in a month for each detector [2]. To measure the dispersion in the response of the fiber- and the trapezoidal detectors, the following measurements have been made by using four pairs of neighboring detectors (one each of fiber- and trapezoidal-type). As mentioned earlier in Section 1 the detectors are deployed on a hexagonal pattern. In the labeling scheme used each detector is assigned a number; the central detector is labeled 1 and the first ring of 6 detectors are labeled 2–7, second ring of 12 detectors are labeled 8–19 and so on. Therefore, a pair of successively numbered detectors are located closest to each other with a separation of only 8 m.

The fractional deviation in the particle density is calculated from its mean value over the range of 3–20 particles m^{-2}. The four detectors are used to determine the mean value at a given density. Over this region (3–20 particles m^{-2}) of particle density, the PMT response is linear for both types of detectors. The results of this study are shown in Fig. 15, for the four pairs of detectors namely, (38,39), (40,41), (42,43), and (58,59). It is clear that the dispersion in the response of the fiber detectors is relatively smaller, as compared to the trapezoidal detectors. Also the response of the four fiber detectors (38,40,42,58) are very similar to each other, and the fractional deviation in the particle density is $\lesssim$2.5%, whereas it is $\lesssim$5.5% for the trapezoidal detectors. However, even a variation of 5.5% is fairly small. Although, the response of the trapezoidal detectors is found to be satisfactory, but the performance of the fiber detectors is comparatively superior.

As mentioned earlier in Section 1, an efficient detector system should provide a large separation between the PMT noise and the signal due to the charged particles in the EAS. In Fig. 16 the ADC distributions obtained using muons passing through two detectors namely; (a) #7 a trapezoidal shaped detector and (b) #10 a WLS fiber detector are shown. The separation between the pedestal and the single particle peak is significantly larger in the case of the new fiber detector (Fig. 16b) as compared to the older trapezoidal detector (Fig. 16a).

The calibration of the low-gain PMT for a single particle is not a viable option, because the PMT operating at such a low-gain would

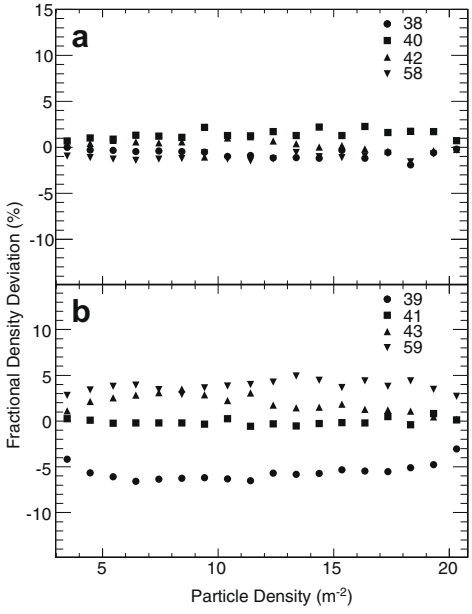

Fig. 15. Fractional variation in measured density as a function of detected particle density: (a) fiber detectors 38, 40, 42, 58 (b) trapezoidal detectors 39, 41, 43, 59. Detectors in each pair (38,39) (40,41), etc. are neighbors, located within ring #4 in the array.

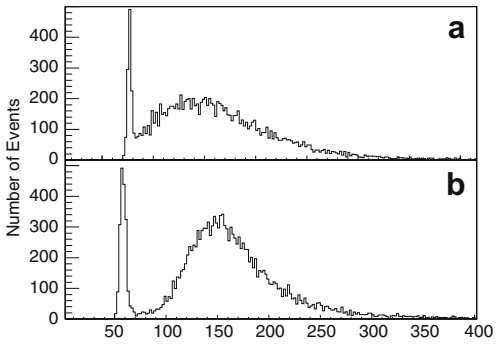

Fig. 16. ADC distributions for passing muons for; (a) old trapezoidal shaped detector #7, (b) new WLS fiber detector #10.

give too few ADC counts, to separate the single particle peak from the pedestal. Therefore, the calibration of the low-gain PMT is extracted indirectly, from the air shower data as detailed below. After subtracting respective pedestals, a ratio of the high- and low-gain PMT ADC counts is calculated for each air shower event. A mean of this ratio (HLR) is calculated in steps of 50 ADC counts of the high-gain PMT. The mean ratio 'HLR' is plotted as a function of the high-gain PMT ADC counts, as shown in Fig. 17 for detector numbers 16, 42, 92, and 94. The flat horizontal region in each plot, corresponds to the common linear domain for both the high- and the low-gain PMTs. This flat region is fit to a straight line parallel to the *X*-axis and its intercept on the *Y*-axis provides, the ratio of the gains of the high- and low-gain PMTs in the detector. Based on the data shown in Fig. 17 a precision of about (1–2)% is obtained in the calibration of the low-gain PMTs relative to high-gain PMTs. However, this value is uncertain to about 5% due to the accuracy of the absolute calibration obtained from single muons for the corresponding high-gain PMT.

At the lower particle densities, the low-gain PMT becomes relatively insensitive, while at higher densities the high-gain PMT starts to saturate. Therefore, the ratio of the high-gain to the low-gain ADC counts shows a reduction, both at small and large particle densities. Using the single particle calibration for the high-gain PMT, and the extracted single particle gain as described above for the low-gain PMT, the observed integral particle density

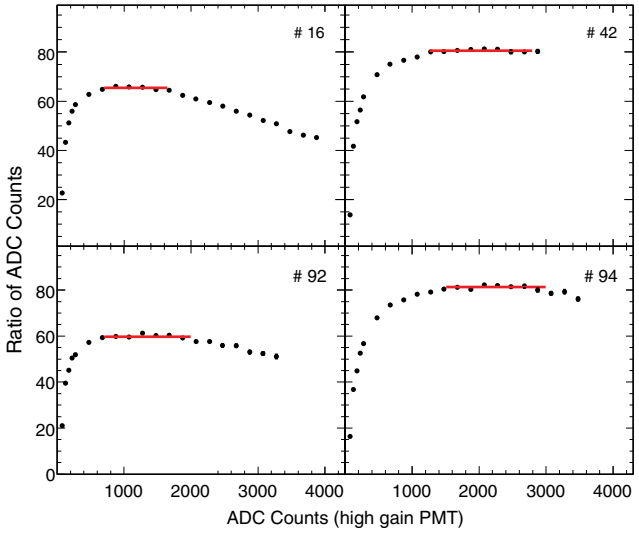

Fig. 17. Ratio of ADC values for 'high' and 'low' gain PMTs as a function of high-gain PMT ADC value. Each data point is the mean value of this ratio for 50 ADC channels. Straight line is a fit to the horizontal region in each plot.

spectrum for the GRAPES-3 experiment has been obtained. The integral particle density spectra for detectors 18, 58, 96, and 100 are shown in Fig. 18. For the low-gain PMTs, the density spectrum is shown only above 10 particles m^{-2}, as the value of the density is rather uncertain below this threshold. In the case of the high-gain PMT the response becomes non-linear above a density of ~50 particles m^{-2} and it saturates in the region of (100–300) particles m^{-2}. On the other hand, the low-gain PMT response remains linear up to ~5000 particles m^{-2} and no saturation is observed. Thus the combination of two PMTs allows the dynamic range of the fiber detector to be extended from 1 to 5000 particles m^{-2}. For most of the detectors the gain ratio of the high- and the low-gain PMTs, is adjusted to be (20–100) with a mean value of ~50. For determining the density spectrum of the particles in the air showers, we have used the data from the high-gain PMTs for the densities below 20 m^{-2} and the low-gain PMTs for the densities above this value.

6. The density spectrum and EAS attenuation

The integral density spectrum of particle measured by the dual-PMT fiber detectors has been obtained to validate the design of these new detectors. The limited dynamic range of the earlier trapezoidal shaped detectors had restricted the maximum detectable particle density to only about 200 m^{-2}. However, with the new dual-PMT detectors this range has been extended to nearly 5000 particles m^{-2} allowing meaningful measurements of density spectrum of particles in the EAS and their attenuation length.

The integral particle density spectra for four dual-PMT fiber detectors namely 18, 58, 96, 100, respectively are shown in Fig. 19. The successive spectra have been shifted downwards, by a factor of 10 for the sake of clarity. All four spectra display a power law behavior and a fit for the density range from 5 to 500 particles m^{-2}, yields a spectral slope of (1.57 ± 0.04), consistent with the early measurements [11,12]. These values are also close to the slope of the energy spectrum of the primary cosmic rays, as has been pointed out in the past [11]. The nearly identical power law spectral index for all four detectors, indicates that the dual-PMT detectors are performing with a reasonably linear response, free from the effects of any saturation.

The zenith angle distribution of the EAS in different intervals of shower size has been studied in the past, to measure the absorption of the EAS in the atmosphere for the primaries of different energies. The ARGO–YBJ collaboration have argued that the measured particle density is due to the contribution of the showers

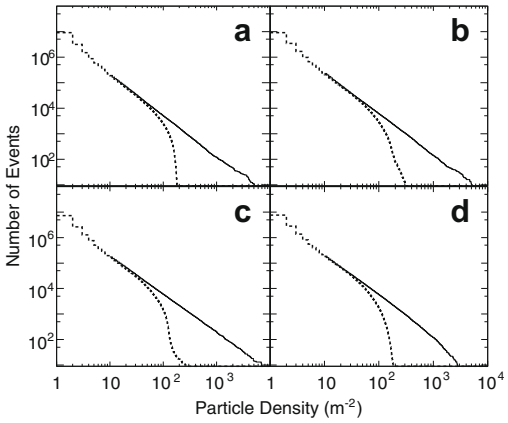

Fig. 18. Integral density spectrum from GRAPES-3 showers for high- and low-gain PMTs of dual-PMT fiber detectors for data from 1 March to 29 May 2005. Detectors: (a) 18, (b) 58, (c) 96, and (d) 100. High-gain PMT shown by a dashed line and low-gain by continuous line.

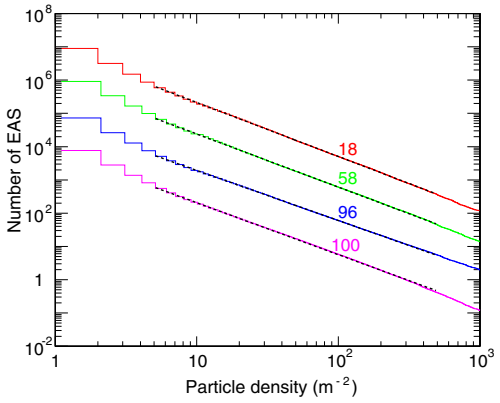

Fig. 19. Integral density spectra for 4 dual-PMT detectors namely 18, 58, 96, 100, respectively, for data from 1 March to 29 May 2005. Power law fit to spectra from 5 to 500 particles m^{-2} yields spectral index $\gamma = 1.57 \pm 0.04$. Successive plots shifted downwards by factors of 10 for clarity.

within a very broad range of shower sizes, and the study of the angular distribution of the events with particle density exceeding a given value is considered, as appropriate as any other parameter such as the shower size. It has been suggested that the angular distribution should display an exponential dependence. Following the equation (2) in reference [15],

$$I(\geqslant \rho,\theta) = I(\geqslant \rho,0)\exp\left(-\frac{X}{\Lambda_a}(sec\theta - 1)\right) \quad (4)$$

where, ρ is the particle density, θ the zenith angle, X the vertical atmospheric depth, and Λ_a the attenuation length of the EAS for particle density $\geqslant \rho$. Using the angular distribution of the EAS with density $\rho \geqslant 3$ particles m^{-2}, the ARGO–YBJ data could be fit to Eq. (4) up to a zenith angle $\theta = 55°$. A value of the attenuation length $\Lambda_a = (124 \pm 11)$ g cm^{-2} was derived for an observational depth of 606 g cm^{-2} [15]. The KASCADE collaboration has studied the attenuation of the EAS in great detail at the sea level as a function of the shower size and the zenith angle. They have obtained a value of the attenuation length $\Lambda_a = 100$–120 g cm^{-2} [16]. Similar results have also been reported by other groups [27,28].

The integral density spectra obtained, by combining the data from the 10 dual-PMT detectors taken over the 3 month interval, are shown in Fig. 20 for 4 different zenith angle intervals namely; (a) $1.0 < sec\ \theta < 1.1$, (b) $1.1 < sec\theta < 1.2$, (c) $1.2 < sec\theta < 1.3$ and (d) $1.3 < sec\theta < 1.4$. Power law fits to the data shown in Fig. 20, for the density range 5–500 particles m^{-2}, for these four zenith angle

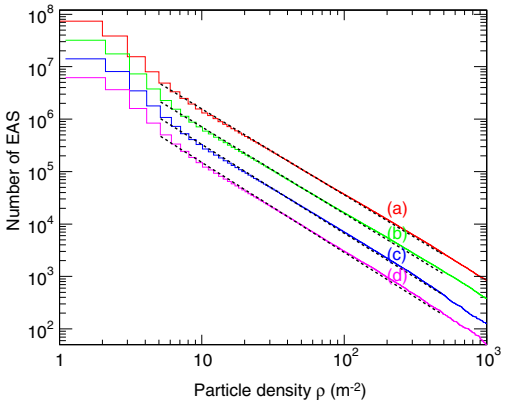

Fig. 20. Integral density spectra using data from 10 dual-PMT detectors for 4 zenith angle intervals; (a) $1.0 < sec\theta < 1.1$, (b) $1.1 < sec\ \theta < 1.2$, (c) $1.2 < sec\theta < 1.3$ and (d) $1.3 < sec\ \theta < 1.4$.

intervals are shown by dashed line. The magnitude of the spectral index γ shows a small, but gradual increase with the increasing zenith angle. The fitted values of the spectral index γ are 1.64, 1.65, 1.69, 1.71 for the four zenith angle intervals listed above. A similar behavior has also been reported earlier [29].

The data for the same period of three months (1 March–29 May 2005) have been used to calculate the number of the EAS as a function of sec $\theta - 1$ in steps of 0.02, where θ is the zenith angle of the EAS. The dependence of the number of EAS on the function sec $\theta - 1$ is displayed in Fig. 21, for 4 different particle density thresholds namely; $(a) > 5$, $(b) > 10$, $(c) > 20$ and $(d) > 40$ m^{-2}. An excellent exponential fit to the 4 sets of experimental data as shown in Fig. 21, is obtained using Eq. (4). The fits are straight lines, due to the logarithmic scale used for the *Y*-axis in Fig. 21. These fits are used to calculate the value of the attenuation length 'Λ_a' of the EAS at the observational level.

To further study the attenuation of the EAS in the atmosphere, the attenuation length 'Λ_a' is calculated using Eq. (4) and by varying the particle density threshold from 5 to 50 particles m^{-2}. The values of Λ_a as a function of the particle density threshold 'ρ' is shown in Fig. 22. The value of Λ_a gradually decreases from 106 g cm^{-2} at $\rho > 5$ m^{-2} to 98 g cm^{-2} at $\rho > 50$ m^{-2}. The range of $\Lambda_a = 98$–106 g cm^{-2} reported here for an atmospheric depth of 800 g cm^{-2} at Ooty is comparable to the measurement of the ARGO–YBJ collaboration of $\Lambda_a = (124 \pm 11)$ g cm^{-2} for an atmospheric depth of 606 g cm^{-2} in Tibet [15] and $\Lambda_a = 100$–120 g cm^{-2} by the KASCADE collaboration [16].

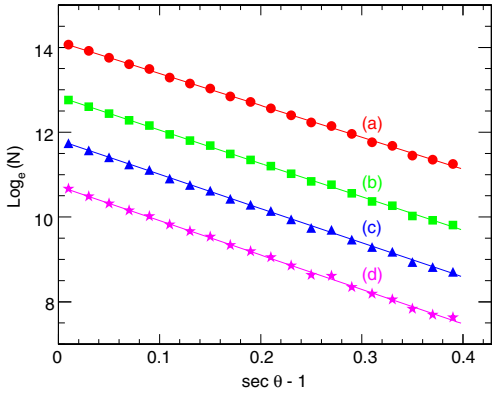

Fig. 21. Number of EAS as a function of sec $\theta - 1$ for 4 particle density thresholds; $9(a) > 5$, $(b) > 10$, $(c) > 20$, and $(d) > 40$ m^{-2}. Straight line fits obtained from Eq. (4).

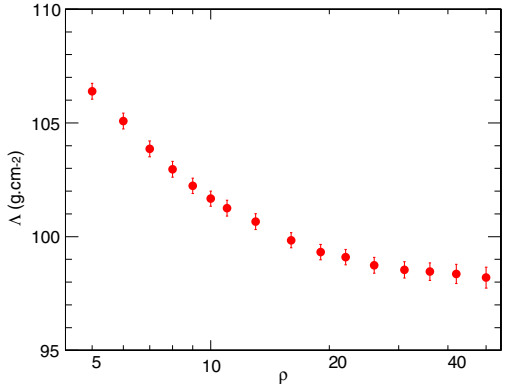

Fig. 22. Variation of the attenuation length Λ_a as a function of the particle density threshold ρ in the range 5–50 m^{-2}.

7. Conclusions

The performance of the newly developed plastic scintillator detectors with WLS fiber readout used in the expansion of the GRAPES-3 experiment has been described in detail. The detector performance in terms of the photon output, the uniformity and the time resolution are in good agreement with the results of the Monte Carlo simulation code G3ScSIM. The use of the WLS fibers has allowed a sizable increase in the photon yield and has also resulted in greater uniformity in the detector response. As a result of this study and due to the simplicity of the fabrication procedure, the *parallel* groove configuration for the layout of the WLS fibers has been used. This resulted in a significant improvement in the performance of the fiber detectors as compared to the old trapezoidal detectors. The dynamic range of the dual-PMT fiber detectors for the measurement of the particle density has increased to $\sim 5 \times 10^3$ particle m^{-2}. This enhanced dynamic range covers the particle densities encountered near the cores of the extensive air showers of energy well above the 'knee' in the spectrum. About 100 dual-PMT fiber detectors are currently operating in the array and more are being continuously added.

The integral density spectrum of the dual-PMT fiber detectors displays a spectral slope $\gamma = 1.57 \pm 0.04$. This value is consistent with the measurements reported earlier in the literature. The zenith angle dependence of the density spectra has been used to estimate the attenuation length 'Λ_a' of the EAS in the atmosphere. The variation in Λ_a, as a function of the particle density threshold has been calculated for the range 5–50 particles m^{-2}. The attenuation length Λ_a is found to vary in the range 98–106 g cm^{-2}, for an atmospheric depth of 800 g cm^{-2} at Ooty. The calculated value of Λ_a is also consistent with the measurements reported earlier.

Acknowledgement

We thank D.B. Arjunan, K. Manjunath, S. Murugapandian, B. Rajesh, C. Ravindran, K. Santosh Kumar and R. Suresh Kumar for their help in the testing, installation and operation of the detectors and the electronic modules. The administrative services of V. Viswanathan during the experiment are acknowledged. We thank A.A. Basha, G.P. Francis, I.M. Haroon, V. Jeyakumar, K. Ramadass, for their help in the fabrication, assembly and the installation of various mechanical components and detectors. The Japanese members of the GRAPES-3 collaboration acknowledge the partial financial support from the Ministry of Education and Science of the Government of Japan for the experiment.

References

[1] S.K. Gupta et al., Phys. Rev. D68 (2003) 052005.
[2] S.K. Gupta et al., Nucl. Instr. Meth. A 540 (2005) 311.
[3] Y. Hayashi et al., Nucl. Instr. Meth. A 545 (2005) 643.
[4] T. Nonaka et al., Phys. Rev. D74 (2006) 052003.
[5] P. Subramanian et al., Astron. Astrophys, in press.
[6] V.I. Kryshkin, A.T. Ronzhin, Nucl. Instr. Meth. A 247 (1986) 583.
[7] D.A. Bukin et al., Nucl. Instr. Meth. A 384 (1997) 360.
[8] S.R. Borenstein et al., IEEE Trans. Nucl. Sci. NS-29 (1982) 402.
[9] A.D. Bross, A. Pla Dalmau, Nucl. Instr. Meth. A 325 (1993) 168.
[10] M. Adams, et al., Nucl. Instr. Meth. A 366 (1995) 263; V. Hagopian, Nucl. Phys. B (Proc. Suppl.) 61 (1998) 355.
[11] K. Greisen, Ann. Rev. Nucl. Sci. 10 (1960) 63.
[12] I. Katsumata, J. Phys. Soc. Jpn. 19 (1964) 800.
[13] R.W. Clay, P.R. Gerhardy, Il Nuovo Cimento 4 C (1981) 26.
[14] D. Ciampa, R.W. Clay, J. Phys. G: Nucl. Phys. 14 (1988) 787.
[15] C. Bacci et al., Astropart. Phys. 17 (2002) 151.
[16] T. Antoni et al., Astropart. Phys. 19 (2003) 703.
[17] Kuraray optical products, Nihonobashi, 1-6,3-Chome, Chuo-ku, Tokyo, Japan.
[18] http://www2.dupont.com/Tyvek/en-US/assets/downloads/tyvek-handbook.pdf.
[19] P.K. Mohanty et al., TIFR/DHEP, Preprint (2008).

[20] L.D. Landau, J. Exp. Phys. (USSR) 8 (1944) 201.
[21] D.H. Wilkinson, Nucl. Instr. Meth. A 383 (1996) 513.
[22] K.S. Kolbig, B. Schorr, Comput. Phys. Commun. 31 (1984) 97.
[23] M. Aguilar-Benitez et al., Phys. Lett. B 170 (1986) 1.
[24] N.S. Kapany, Fiber Optics: Principles and Applications, Academic Press, London and New York, 1967.
[25] W.L. Leo, Techniques for Nuclear and Particle Physics Experiments, Narosa Publishing House, New Delhi, 1995.
[26] M. Moszynski, Nucl. Instr. Meth. A 158 (1979) 1.
[27] D.E. Alexandreas et al., Nucl. Instr. Meth. A 328 (1992) 570.
[28] M. Aglietta et al., Nucl. Phys. B (Proc. Suppl.) 70 (1999) 509.
[29] J.D. Hollows, H.W. Hunter, A.N. Suri J. Phys. A: Gen. Phys. 2 (1969) 591.